Multiannual Change Detection in Long and Dense Satellite Image Time Series Based on Dynamic Time Warping

Khatereh Meshkini, *Member, IEEE*, Yady Tatiana Solano-Correa, *Member, IEEE*, Francesca Bovolo, *Senior Member, IEEE*, and Lorenzo Bruzzone, *Fellow, IEEE*

***Abstract*— High-resolution (HR) satellite image time series (SITS) are a valuable data source for analyzing land cover change (LCC) due to their large amount of spatial, spectral, and temporal information. However, most existing LCC detection methods focus on binary change detection (CD) within a single year and fail to provide detailed information about the specific type of change. In this study, we propose a multiannual CD approach that identifies changes occurring between consecutive years and provides information about the type of LC transition. The proposed approach exploits multiannual and multispectral SITS to generate a hypertemporal feature space (FS). This FS is analyzed to create a set of CD maps that indicate the time, probability, and type of change. To measure the similarity between pixel time series, we use dynamic time warping (DTW) in the space of hypertemporal features. A hierarchical clustering technique is exploited to develop a set of class prototypes (CPs) that represent the characteristics of different LC classes. The CPs are then used to identify the most probable LC transition for each changed pixel. Two test areas were selected to evaluate the effectiveness of the proposed approach. The first one is located in Amazon and spans the years 2015 to 2019; and the second one is located in Sahel-Africa and covers the years 2015 and 2016, using multiannual Landsat 7 and 8 SITS. The results demonstrate that the proposed approach is effective in detecting multiannual changes and in identifying the LC transitions.**

***Index Terms*— Dynamic time warping (DTW), hypertemporal feature, land cover change (LCC), land cover (LC) transition, multiannual, remote sensing (RS).**

I. Introduction

LAND cover (LC) analysis is a very attractive research field that aims to support the proper planning and utilization of natural resources and their management. There is a direct link between the availability of information and adequate LC planning for successful and sustainable LC management.

Due to the increased number of remote sensing (RS) satellites and the availability of high spatial and temporal resolution (HR) images, a new era is initiated in the area of satellite image time series (SITS) analysis. Detailed spatial, spectral, and temporal information provide capabilities for effective monitoring of landforms, vegetation, and land use (LU) to support climate modeling research [1], [2]. Moreover, the possibility of using multiannual multispectral SITS opens the door to properly characterize the LC features between the extreme instances (years) and analysis of climate change causes and effects such as urbanization [3], industrial operations, natural disaster [4], and deforestation [5]. Several studies have been carried out to analyze and monitor LU and LC on Earth surface by utilizing multitemporal satellite images. Some of them focused on analyzing the multitemporal behavior of the LC and extracting important phenological features. A tool developed in [6] that produces phenological information from satellite vegetation index time series. The method extracts the main growing season information, estimates double growth season parameters, and can select temporal regions of interest. A study exploited multitemporal satellite images for crop mapping together with the estimation of the crop dynamics [7]. The method performs a boundary detection to separate the crop fields based on their phenological behavior and estimates of phenological parameters, such as the number of cropping cycles, the length of season, the middle of season, and the maximum value of temporal signature. The study focuses on agricultural areas characterized by irregularly sampled seasonal time series data, specifically targeting small-scale and intensively cultivated crop fields.

Some methods detect LC Change (LCC) by developing algorithms that can process longer temporal samples and thus better model temporal evolution [8], [9]. Others deal with the long-time scale high temporal resolution case (i.e., multiannual SITS), by analyzing changes over consecutive years [10]. The research in [11] used normalized difference vegetation index (NDVI) to find changes in the mountain using Landsat images. Each image in multitemporal SITS underwent supervised classification based on the extracted features. Some methods involve separate images for each time period to generate object-based maps of the study area. These

Manuscript received 16 November 2023; revised 1 June 2024; accepted 5 July 2024. Date of publication 22 July 2024; date of current version 8 August 2024. This work was supported in part by European Space Agency (ESA) Climate Change Initiative (CCI+) New Essential Climate Variables (ECVs) High Resolution Land Cover (HRLC), under Contract 4000125259718/I-NB. *(Corresponding author: Francesca Bovolo.)*

Khatereh Meshkini is with the Center for Digital Society, Fondazione Bruno Kessler, 38123 Trento, Italy, and also with the Department of Information Engineering and Computer Science Trento, University of Trento, 38123 Trento, Italy (e-mail: mkhatereh@fbk.eu).

Yady Tatiana Solano-Correa is with the Facultad de Ciencias Básicas, Universidad Tecnológica de Bolívar, 130001 Cartagena, Colombia (e-mail: solanoy@utb.edu.co).

Francesca Bovolo is with the Center for Digital Society, Fondazione Bruno Kessler, 38123 Trento, Italy (e-mail: bovolo@fbk.eu).

Lorenzo Bruzzone is with the Department of Information Engineering and Computer Science Trento, University of Trento, 38123 Trento, Italy (e-mail: lorenzo.bruzzone@unitn.it).

Digital Object Identifier 10.1109/TGRS.2024.3431631

maps are compared to detect changes in the objects using a change detection (CD) index based on the difference features [12]. In this context, a CD algorithm is proposed in [13] that compares the classified images of different time periods to detect changes associated with LULC. Wang et al. [14] introduced a CD method based on the normalized difference indices (NDI) of fused multitemporal images. The method combines fused images and spectral distortion measures to increase the accuracy of CD.

One of the most popular techniques in multiannual data analysis is segmenting the time series into piecewise linear parts [15]. The time span is divided into intervals, corresponding to the repetitive LC trends in the observed data [16], [17]. The number of intervals is determined by the number of expected trend changes, and it can be related to seasons, years, or multiyears. Among others, we recall the exponentially weighted moving average EWMACD [18], a harmonic regression-based kernel approach for detecting any persistent deviation from a steady pattern seen over the temporal period. In areas where the LC variation is periodic in the time series, this technique performs very well. However, it has limitations when applied to time series with aperiodic changes and/or unstable training periods. Breaks for additive seasonal and trend (BFAST) [19] is more general and models both linear trends and seasonal variations. BFAST periodic linear model is more accurate since it recursively evaluates the possibility of every single time point being a breakpoint, and then chooses the optimal set of breakpoints. BFAST is mainly exploited on medium spatial resolution SITS and in the most cases, it considers the NDVI or a few vegetation indices [20]. It provides information on the time of the occurrence of abrupt changes, without detecting the LC transitions. An effort is required to design a LC CD technique that can effectively process HR SITS to derive information on both the presence of the changes and the LC transitions between the years at multiannual scale.

Developing a methodology that is able to illustrate the LC transitions requires complex algorithms that properly detect the evolution of LC classes. Efforts have been placed on methods utilizing distance measurements to discern differences between LC categories and identify transitions, such as the approaches based on the Euclidean and the Mahalanobis distances [21]. In response to the need for improved distance measurement methods, a variant of change vector analysis (CVA) has been developed to specifically account for both the magnitude and direction of change vectors, with a particular focus on bitemporal CD scenarios [22]. Traditional distance measurement techniques, such as standard CVA, often struggle to effectively capture the dynamic behavior of LC over time. In such cases, incorporating alternative approaches like modified CVA [23] and dynamic time warping (DTW) can more effectively handle and interpret the complexities inherent in time series data. In time series data mining research, methods based on DTW have shown to be effective in a variety of applications [24], [25]. Because of its capacity to define the optimal alignment of radiometric trends, DTW can mitigate the temporal distortions and compare shifted RS time series even if they are irregularly sampled [26]. In [26], the author demonstrates its relevance in handling cloud-contaminated SITS. It shows how DTW can jointly cluster data from different years, exploiting the cyclic behavior of land surface, generate clusters for 1 year and apply them to another year with different acquisition dates. Moreover, it can handle high temporal resolution SITS. It has been successfully applied to SITS analysis in critical conditions such as inadequate training samples and irregular phenological behavior of LC [27], [28]. An object-based time-weighted DTW is developed in [29] that investigates the DTW performance for cropland mapping using objects as spatial analysis units. However, given the DTW unique capacity to determine sequence similarity metrics, a few DTW-based LC-driven CD techniques on multiannual satellite images have been developed.

In this article, we propose an effective LC CD technique for processing HR multiannual multispectral SITS to derive LC transition information between consecutive years. The proposed approach employs three datasets, one for training and the others for testing. The CD process is performed based on the assumption that there is a change over the time series. Thus, two LC maps that represent the initial and final dates of the time series are exploited to generate a post classification comparison (PCC) map to identify candidate changed and unchanged pixels and reduce the computational burden. Additionally, the proposed technique incorporates abrupt CD to further detect changed pixels. The candidate changed pixels are used in the testing steps to proceed with LC transition detection for testing datasets. The approach assigns samples in the training dataset to specific class clusters and generates a set of CPs to map LC transitions in the testing datasets. The CPs model the behavior of LC transition classes assuming stationarity over time. These samples are associated with a label derived from PCC map. To generate the CPs, the training step performs a similarity analysis by using a hierarchical clustering using DTW. DTW is exploited to merge or split class clusters by calculating the similarity metrics in multiannual SITS accounting for temporal differences like seasonal variations that affect LC transition interpretation. The CPs are then used to determine the LC class associated with each changed pixel in the testing dataset for each time interval corresponding to each year. Recognition of the LC class for each year leads to identification of the LC transitions within multiannual SITS.

The proposed method can be summarized in five steps: 1) information extraction from multiannual multispectral SITS; 2) multifeature time series regularization to have a uniform and denser time sampling; 3) abrupt CD using multifeature hypertemporal CVA (MHCVA) followed by a break point detector; 4) CPs evaluation based on DTW; and 5) CD maps generation considering the LC transitions for each changed pixel. The proposed approach provides information of the time of changes, the probability of a given change, and the yearly LC transition for each pixel with an abrupt change in long-term SITS. We evaluated our proposed approach using Landsat data in South America where deforestation occurred between 2015 and 2019 and in Sahel-Africa from 2015 to 2016 with various kinds of LC changes. The rest of this article is organized as follows.

The proposed approach to CD in SITS based on DTW algorithm is presented in Section II. Section III illustrates

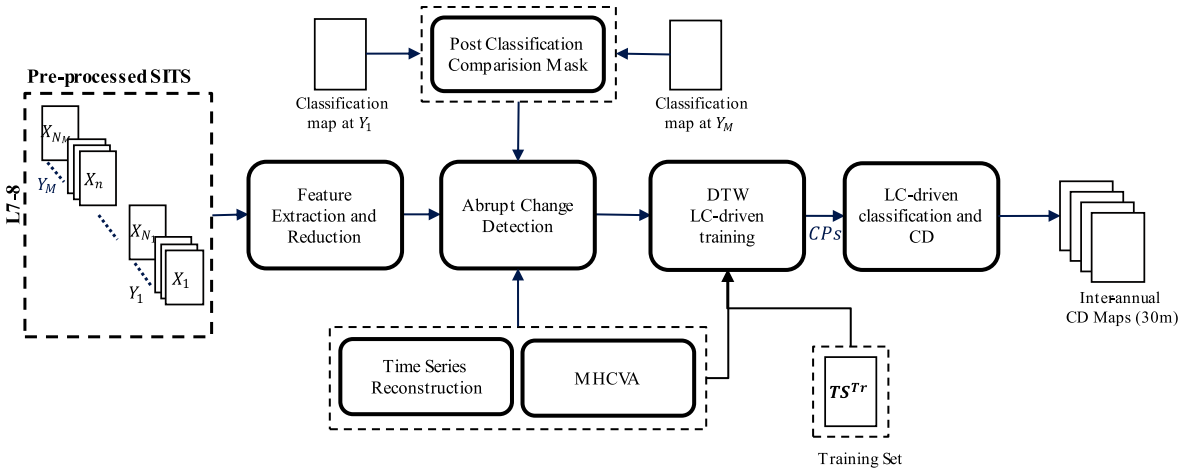

Fig. 1. Block scheme of the proposed DTW-based approach to CD in SITS.

the study area and the experimental results. Section IV provides the discussion and conclusion on the scope of future development.

II. Proposed Approach to CD in SITS Based on DTW

The proposed approach aims to establish a multiannual class similarity analysis for identifying LC transitions. Let SITS $= \{Y_1, Y_2, \ldots, Y_m, \ldots, Y_M\}$ be a SITS comprising M years being preprocessed to filter out cloudy pixels (e.g., exploiting Google Earth Engine - GEE [30]). Each year $Y_m = \{X_1, X_2, \ldots, X_n, \ldots, X_N\}$ consists of several images over the same geographical area with nonuniform time sampling. Let $B = \{b_1, b_2, \ldots, b_K\}$ be the set of K bands that compose the multispectral images. Each image $X_n \in Y_m$ has a total number of P pixels and represents the surface reflectance in a given spatial position at a given time. Fig. 1 shows the block scheme of the proposed approach. It uses the preprocessed SITS from Landsat 7 and 8 sensors to extract the spectral–temporal features of different sets of LCs. Assuming that two LC maps are available for the first and the last year of the analyzed time interval, the changed pixels are identified by a PCC technique and are exploited in the MHCVA and the break point detector to produce an abrupt CD map. DTW LC-driven training identifies the LC trends, and finally LC-driven classification and CD produce the final LC transition map that indicates the year of change and identifies the LC transition for each time frame.

A. Feature Extraction and Reduction

The first stage is crucial and consists of determining a suitable feature space (FS) to distinguish the spectral trends of various sets of LCs. The combination of the spectral bands acquired by the optical sensor provides suitable information to analyze the LC behavior in SITS [31]. Each combination is sensitive to specific LC properties or phenomena, such as vegetation cover, water bodies, or bare soil, and combining them can capture a wider range of LC changes and transitions. This stage transforms the B-dimensional FS into a F-dimensional FS. In our approach, all possible couples of the available sensor bands are considered to compute a set of normalized difference indices NDI_f^{SITS}, $f = 1, \ldots, F$ being able to highlight the interaction between singular bands in emphasizing specific kinds of change, are calculated as follows (The *NDI* indices assume values in the $[-1, 1]$ interval):

$$NDI_f^{\text{SITS}} = \frac{b_i - b_j}{b_i + b_j}, \quad f = (1, \ldots, F) \tag{1}$$

where $b_i, b_j \in B$

$$F = \frac{1}{2}(K-1) \times K. \tag{2}$$

Equation (1) when applied to numerous spectral bands of satellite images, yields a huge number of *NDI*s. Most of them have either unrelated or redundant information. Thus, a feature reduction method is implemented to keep the most informative and reliable features. It is based on the kernel principal component analysis (KPCA) [32] that considers nonlinear relationships in the data while retaining interpretability. In this step, an appropriate kernel function is selected to calculate the kernel matrix for the eigenvalues and eigenvectors computations. Sorting the eigenvalues in descending order and choosing the top *FR* eigenvalues represent the most variance in the features. Thus, a *FR*-dimensional features is generated to preserve the most informative information ($FR < F$).

B. Abrupt CD

Abrupt CD distinguishes between pixels that have undergone changes and those that did not. Assuming the availability of LC maps for the initial and final year within the processing period, a PCC map is generated to segregate unchanged and changed pixels in the pair of Y_1 and Y_M. The selection process improves the reliability of the CD maps while reducing the overall computational burden. The changed pixels are exploited in the testing step for the time series reconstruction module that helps to identify potential intraannual changes. The method involves regularizing the time series to generate a sequence of values with uniform sampling that is denser than the original signal and MHCVA is used to further identify candidate changed pixels.

C. Time Series Reconstruction

Clouds, cloud shadows, and radiometric effects generate missing data and introduce irregularity in the SITS. The gaps

in the SITS decrease the data quality and thus the capability of performing LCC detection. To have continuous and regular SITS in time, a time series reconstruction technique is applied to $NDI_f^{\text{SITS}}, f = 1, \ldots, F$. The choice of the appropriate interpolation approach is critical in this case since it has a direct impact on the CD accuracy [33]. To this end, preliminary symmetrical and consistently sampled $NDI_f^{\text{SITS}}, f = 1, \ldots, F$, are created by filling in the gaps with a linear combination of nearby values. Then, a time series reconstruction method is applied in two steps: 1) NDI_f^{SITS} data imputation by upper envelope and withdrawn strategy and 2) adaptive nonparametric regression of augmented NDI_f^{SITS} based on a multilayer perceptron neural network (MLP-NN) [33]. The use of an MLP-NN allows to capture the unique temporal behavior of ground responses as well as precisely model class behavior complexity that parametric models do not capture. The result is a smooth, regular, and continuous time series.

D. MHCVA

The abrupt CD is based on a MHCVA method [23] that calculates the difference feature magnitude to find the differences between couples of NDI_f^{SITS} in consecutive years. Let us assume NDI_f^{SITS} is divided into records acquired in the same years as $NDI_f^{\text{SITS}} = \{NDI_f^1, \ldots, NDI_f^{Y_m}, \ldots, NDI_f^{Y_M}\}, f = 1, \ldots, FR$. Let $NDI_f^{Y_m}$ and $NDI_f^{Y_{m+1}}$ be the sets of NDIs of feature f for the years Y_m and Y_{m+1} within the SITS. The length of NDIs depends on the frequency of the time series reconstruction (i.e., daily, weekly, or monthly). A difference hyper temporal vector is calculated for each feature by subtracting $NDI_f^{Y_m}$ and $NDI_f^{Y_{m+1}}$ as

$$NDI_f^{Ym,Ym+1} = NDI_f^{Y_m} - NDI_f^{Y_{m+1}}. \tag{3}$$

The features magnitude $\left\|NDI^{Y_m,Y_{m+1}}\right\|$ is computed from the difference multifeature hyper temporal vectors as

$$\left\|NDI^{Y_m,Y_{m+1}}\right\| = \sqrt{\sum_{f=1}^{f=FR}\left(NDI_f^{Ym,Ym+1}\right)^2}. \tag{4}$$

The magnitudes for the neighboring years are stacked one after the other to generate the multiannual feature magnitude NDI^{SITS}. The NDI^{SITS} is exploited as an input for the break point detection based on the BFAST methodology. BFAST has been tested mostly on NDVI and was developed using MODIS data with a focus on forest CD. In this study, we developed the abrupt CD method using an extended version of BFAST that works with both vegetation and nonvegetation classes in NDI^{SITS}.

The output of this step has two change properties: the years of changes and the probability of change. This step further increases the reliability of the CD processing chain since it: 1) filters out the unchanged pixels for a better estimation of the class trend model and 2) filters out changed pixels to produce more reliable change maps representing LC transitions.

E. DTW LC-Driven Training

Once the NDI^{SITS} has been computed, the DTW LC-driven approach is utilized to model the evolution of LC classes and predict the class of the change. Let $TS^{Tr} = \{TS_1, \ldots, TS_p, \ldots, TS_V\}$ be the training set including V time series training samples. All the training samples are associated with one LC class among L possible classes. When dealing with a large amount of data, representing the trend of TS^{Tr} classes often indicate subtrends that can be categorized by subclusters within the classes [34]. The LC training phase aims to prototype alternative trends for the same class by forming clusters of similar TS_p. Then, a set of CPs is created that models the trend of LC clusters and classes. The generation of CPs starts with a similarity measure calculation based on DTW. A similarity matrix SM is generated by computing DTW between all the training samples in TS^{Tr}. A maximum shift value has been established to limit the total number of links between two training sample sequences during the DTW calculation [35]. This is achieved by adjusting the global constraint in the algorithm. A smaller maximum shift value can lead to faster computation but less precise alignment, whereas a larger maximum shift value can result in slower computation but more accurate alignment. It is important to carefully select an optimal value for the maximum shift, considering the trade-off between computational speed and alignment accuracy. The similarity matrix SM is computed as follows:

$$S_{p,q}^{FR} = \text{DTW}(TS_p, TS_q), \quad 1 \le p \le V \quad 1 \le q \le V, p \ne q \tag{5}$$

$$SM^{FR} = \begin{vmatrix} 0 & S_{1,2}^{FR} & S_{1,3}^{FR} & \ldots & S_{1,V}^{FR} \\ S_{2,1}^{FR} & 0 & S_{2,3}^{FR} & \ldots & S_{2,V}^{FR} \\ S_{3,1}^{FR} & S_{3,2}^{FR} & 0 & \ldots & S_{3,V}^{FR} \\ \ldots & \ldots & \ldots & \ldots & \ldots \\ S_{V,1}^{FR} & S_{V,2}^{FR} & S_{V,3}^{FR} & \ldots & 0 \end{vmatrix} \tag{6}$$

where $TS_p, TS_q \epsilon TS^{Tr}$. The matrix is normalized with element values in the [0, 1] as follows:

$$SM^{FR} = \frac{\max\left(SM^{FR}\right) - SM^{FR}}{\max(SM^{FR})}. \tag{7}$$

Large values in the matrix indicate high similarity, whereas small values indicate low similarity. All diagonal elements become equal to 1. SM is used to calculate the set of similarity thresholds $Th = \{Th^1, \ldots, Th^i, \ldots, Th^L\}$ for each LC class. The similarity threshold Th^i for class $i \in \{1, \ldots, L\}$ is calculated considering the following equation:

$$Th^i = \max\left[Th^{i,j}\right] i, \quad j = 1, \ldots, L, \; i \ne j \tag{8}$$

where $Th^{i,j}$ is defined as the similarity threshold between class i and j. To start with similarity analysis, let us consider the vectors in SM belonging to class i (defined as $SM^{i,i}$ with size $a \times a$). We use Gaussian probability density function (PDF) [36] to simplify the approximation of the similarity threshold. It is determined as PDF_i being the PDF of $SM^{i,i}$.

The similarity threshold $Th^{i,j}$ between class i and j ($i \ne j$) is computed considering following Algorithm 1: The algorithm is applied to all the classes in the training set to define a similarity threshold for each class. The clustering algorithm employs $Th = \{Th^1, \ldots, Th^L\}$ to separate different clusters. Moreover, a predefined similarity index S_{idx} is considered

Algorithm 1 Similarity Threshold

$PDF_i \leftarrow$ probability density function of $SM^{i,i}$ *with size* $a \times a$
$PDF_j \leftarrow$ probability density function of $SM^{i,j}$ *with size* $a \times b$
$mean_i \leftarrow$ mean value of Gaussian PDF_i
$mean_j \leftarrow$ mean value of Gaussian PDF_j
$S_d \leftarrow$ decrease step value for the similarity measure
$Th \leftarrow$ similarity threshold
for *each* $n \in \{1, 2, \ldots, a\}$ **do**
  if $mean_i^n \geq mean_j^n$ **then**
    while $PDF_i[mean_i^n] - PDF_j[mean_j^n] \geq 0$ **do**
      $mean_i^n = mean_i^n - S_d$
    end
    $Th^{ij} = mean_i^n$
  end
end

which is determined based on the maximum similarity value. The S_{idx} is an adaptive value that starts as the maximum similarity value and gradually decreases until it reaches the convergence threshold, Th. The parameters P_A and P_B impose the minimum number of samples per cluster and the maximum number of clusters per class (which is determined considering the total number of training samples for each class), respectively. The clustering process includes the following steps.

1) The first training sample creates a new group. Let $\Theta^i = \{\Theta_1^i, \Theta_2^i, \Theta_3^i, \ldots, \Theta_Q^i\}$ be the present set of clusters for the class i.
2) The similarity measure between each training sample and the cluster prototype is computed. If it exceeds S_{idx}, then the sample can be included in the cluster (in the case of multiple suitable clusters, the one with the highest average similarity is selected). Else, a new cluster will be created.
3) The process is iteratively repeated until all the samples have been assigned to clusters.
4) After processing all the samples, the clusters Θ^i are evaluated to determine if the generated group of samples satisfies the specified parameter constraints P_A and P_B. If the parameter check is unsuccessful, then the S_{idx} is decreased by S_d and a new set of clusters is produced. Else, the clusters drive the computation of the CPs.
5) For each cluster Θ_q^i, the sample values are averaged to create a set of clusters for class i as $\{CP^i = CP_1^i, \ldots, CP_q^i, \ldots, CP_Q^i\}$.

The class prototype (CP) generation is performed for all the classes to have a set of prototypes $CP = \{CP^1, \ldots, CP^i, \ldots, CP^L\}$ with several clusters for each class representing the different behaviors of LC classes. This ensures the creation of prototypes for the innerclass behaviors, as well as the recognition of different LC trends within classes.

F. LC Classification and CD

The CPs created during the LC training stage are employed as a class trend model to identify the LC transition of each pixel associated with a spatial position in the testing dataset. This stage qualifies the reliability of the CPs in determining the LC classes. The assumption is that the characteristic of the testing dataset is almost similar to the training dataset to be able to properly classify different LC classes associated with CPs. Let $TS^{Te} = \{TS_1, \ldots, TS_p, \ldots, TS_W\}$ be the testing set including W samples. Assume $TS_p^{Te} = \{TS_p^{Y_1}, \ldots, TS_p^{Y_m}, \ldots, TS_p^{Y_M}\}$ is a candidate change pixel in the testing dataset with a time series of values from Y_1 to Y_M. All TS_p^{Te} are associated with a LC class for each Y_m, ensuring the availability of at least one LC transition during the whole-time span. The DTW similarity measure is evaluated between CPs and each $TS_p^{Y_m}, 1 \leq m \leq M$ to detect the similarity between the unknown pixels and known LC behaviors.

Given $TS_p^{Y_m}$ and CP_q^i for class i and cluster q, the DTW similarity measure S_p^i is defined as

$$S_p^i = \mathrm{DTW}\left(TS_p^{Y_m}, CP_q^i\right), \quad 1 \leq m \leq M \quad 1 \leq i \leq L, \quad 1 \leq q \leq Q. \tag{9}$$

The operation is repeated for all L classes and Q clusters, generating a class similarity vector S_p. The maximum value of S_p indicates the class to which the pixel p belongs for the year Y_m. The process is continued for all years to determine the LC classes of pixels in TS^{Te}. The procedure concludes with the creation of a series of CD maps that highlight LC transitions from one class to another over specific yearly time intervals.

III. Study Area and Experimental Results

A. Datasets Description

The proposed approach is trained on an area in South America and tested on two areas, one in South America and the other in Sahel-Africa.

1) Training Dataset: It is located in the West-Central Amazonian rainforest area of Brazil. The size of the training area is 400 × 400 px (12 × 12 km). A total of 136 cloud free Landsat 7 and 8 images were considered acquired over a 5-year period from January 1st, 2015 to December 31st, 2019. The location is in close proximity to Anastácio city, with the Aquidauana river flowing North of the city, ensuring a diverse range of LC classes [Fig. 2(a) and (b)].

2) Testing Dataset 1: It is located in Paraguay where several crop fields have been built after deforestation in 2015 (Y_1)–2019 (Y_M). The prominent change class is the transition from trees to grassland/cropland that can be easily identified by comparing images from different years. Overall, 116 Landsat 7 and 8 images with size of 600 × 600 px (18 × 18 km) were selected [Fig. 3(a) and (b)].

3) Testing Dataset 2: It is located in Sahel-Africa and shows several kinds of changes and thus more complex behavior with respect to testing dataset 1. The undergoing changes are the formation of several central pivot crops, the construction of buildings, and the transition from crop to bare land (Fig. 4). The size of the area is 600 × 600 px (18 × 18 km), and the SITS includes 25 Landsat 8 images acquired in 2015 (Y_1)–2016 (Y_M). The testing dataset 2 in Sahel-Africa is used to evaluate the performance of the proposed approach while processing an area showing different types of LC transitions from both the training dataset and the testing dataset 1.

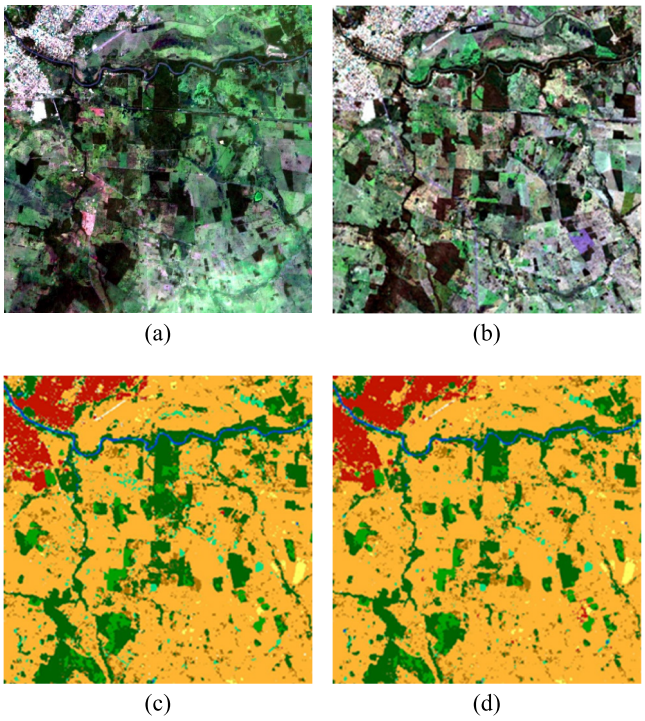

Fig. 2. (a) and (b) Examples of RGB image of the training dataset for the years 2015 and 2019. (c) and (d) Available LC maps for the years 2015 and 2019.

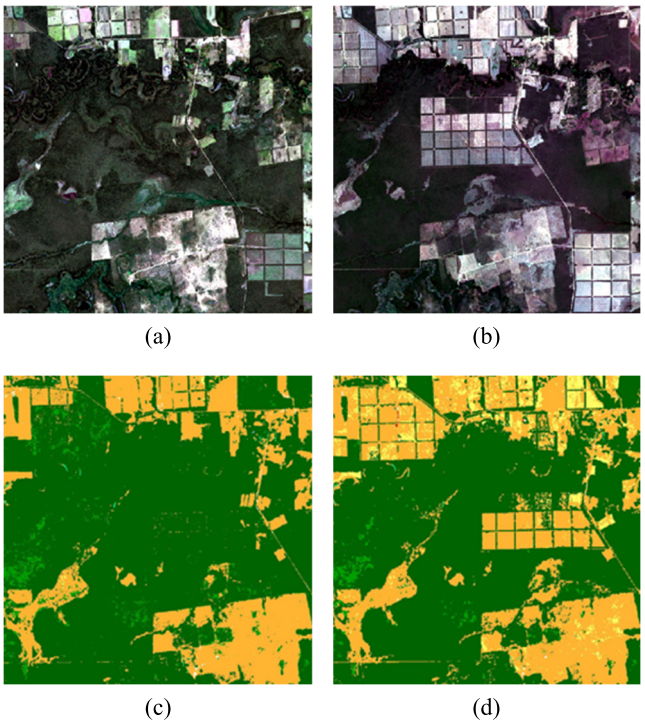

Fig. 3. (a) and (b) Examples of RGB image of the testing dataset 1 for the years 2015 and 2019. (c) and (d) Available LC maps for the years 2015 and 2019.

The datasets were obtained directly from GEE [37], which offers access to the USGS Landsat Collection 2 surface reflectance dataset. This comprehensive collection contains atmospherically corrected surface reflectance data captured by the Landsat 7 ETM+ and the Landsat 8 OLI/TIRS sensors. Landsat collection 2 includes various enhancements

Fig. 4. Example of RGB images of testing dataset 2 for the years (a) 2015 and (b) 2016.

TABLE I
TRAINING AND TESTING LEGENDS

Training legend		Testing legend	
1	Evergreen Broadleaf	1/2	Trees
2	Deciduous Broadleaf		
3	Shrub	3	Shrub
4	Grassland	4	Grassland
5	Cropland	5	Cropland
6	Vegetation Aquatic	6	Vegetation Aquatic
7	Bare Areas	7	Bare Areas
8	Built Up	8	Built Up
9	Water	9	Water

in geolocation, radiometric calibration, and atmospheric correction thereby improving efficiently processing Landsat datasets [38].

The Landsat collection 2 reflectance calibration is maintained with a low absolute reflective spectral band calibration uncertainty, thus allowing to obtain a homogeneous SITS, even if acquired by different Landsat sensors [39]. Here, the LC map for the LC-driven training is the one produced for 2019 as a part of high-resolution LC (HRLC) climate change initiative (CCI+) project [Fig. 2(d)] [40]. HRLC CCI+ products are freely accessible HR (10/30 m) LC and CD maps at subcontinental/regional level. The LC-driven training legend includes the nine classes described in Table I.

The PCC map needed for training was generated exploiting the abovementioned 2015 and 2019 maps [Fig. 2(c) and (d)]. The same has been used to drive abrupt CD in testing dataset 1 [Fig. 3(c) and (d)]. To evaluate the method performance, the dynamic world (DW) LC maps [41] were employed to generate the reference change/transition maps for each year in testing dataset 1.

DW is a free global 10 m resolution LC dataset, downsampled to 30 m resolution using the majority voting strategy in 3 × 3 windows. The testing DW LC map legend shows eight classes, including trees, shrub, grass, crops, flooded vegetation, bare, built-up, and water (Table I). Therefore, evergreen broadleaf and deciduous broadleaf classes were merged into trees class for performance assessment. DW product has been used to generate the PCC map for abrupt CD and for

TABLE II
NUMBER OF SAMPLES FOR EACH CLASS IN THE TRAINING SET

Class Number	Number of the samples
Evergreen broadleaf	9336
Deciduous broadleaf	4410
Shrub	8304
Grassland	20683
Cropland	1297
Vegetation aquatic	1787
Bare areas	256
Built up	8022
Water	962

TABLE III
CLASSES AND CORRESPONDENT SIMILARITY THRESHOLD VALUES

Class Number	Similarity Threshold (Th)
Evergreen broadleaf	0.8209355
Deciduous broadleaf	0.8594567
Shrub	0.8347914
Grassland	0.8189867
Cropland	0.8292946
Vegetation aquatic	0.8477301
Bare areas	0.8209359
Built up	0.8001654
Water	0.7706452

the reference change/transition maps for testing dataset 2. The reference map points out that there are no trees or grass class in testing dataset 2. The PCC mask is generated between 2015 and 2016 using the first free image of 2015 and the last one in 2016.

B. Training Phase

To proceed with the LC-driven training, the training dataset SITS were transformed into *NDI*s using (1). By considering the number of Landsat spectral bands ($K = 6$), (2) produced a total of $F = 15$ features. To handle the computational time and preserve the features more sensitive to change, the Gaussian KPCA [33] was applied to the 15 features that transform the features into kernel-induced FS. The weight for each original feature was calculated by projecting the data points onto the chosen principal component and then mapping these projections back to the original FS. The three most informative features being NDVI, (SWIR1, NIR) and (SWIR2, Blue) remained for further analysis. The PCC identified pixels with a high probability of no change during the training phase and pixels with a high probability of change during the testing phase.

In the training dataset, there were a total of 149 408 unchanged pixels, out of which approximately 98 500 samples belong to class 7 (grassland). To alleviate the computational burden, a random selection of around 21 000 samples from class 7 was made to model the class trends. As a result, there were 55 000 samples across nine classes, as shown in Table II. To transform the original temporal signal into a harmonized and continues sampling sequence, a weekly time series reconstruction procedure was implemented as described in Section II-C. A prior analysis has shown that reconstruction of one sample per week guarantees a reliable detection of yearly changes and reduces the computational time dramatically [42]. Then, multiannual feature magnitude was calculated using the MHCVA method. For the training, the similarity matrix SM was computed using the maximum shift value of 15 weeks. The value was chosen considering possible moderate seasonal shift. The SM matrix was normalized to a range of [0, 1]. Following Section II-E, it is possible to compute Th^i for each of the classes in SM. Table III shows the classes and the similarities threshold values. Optimized P_A and P_B values resulted to be 0.005% and 0.01%, respectively. S_{idx} starts from the highest value, 1, and decreases by $S_d = 0.001$ to reach Th^i for each class. After all the clusters for each class were determined, a set of CPs for each cluster was generated to represent the behavior of each class.

TABLE IV
CONFUSION MATRIX. PA, UA, AND OA (%)

	1	2	3	4	5	6	7	8	9	UA%
1	17156	915	1502	1020	134	120	11	451	12	80
2	4457	3176	115	256	55	47	8	39	15	39
3	1354	103	5323	814	107	31	9	1166	9	60
4	336	54	621	14126	173	98	9	653	23	87
5	452	87	522	3373	754	37	7	128	38	14
6	318	37	154	204	20	1121	5	117	60	55
7	28	7	8	38	35	10	171	22	0	54
8	524	10	51	730	12	22	32	5417	4	80
9	152	21	8	122	7	301	4	29	801	55
PA%	69	72	64	68	58	62	67	67	83	68

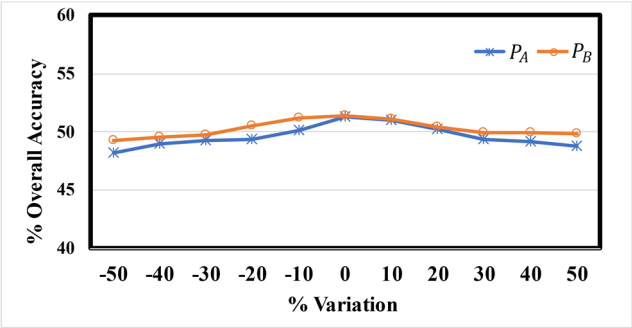

Fig. 5. Overall accuracy (%) of sensitivity analysis for P_A and P_B.

The accuracy of the CP models was evaluated by performing LC classification. This was done by calculating the DTW similarity measure between all the samples in TS^{Tr} and the CPs for each class. The maximum DTW similarity value indicates the class to which the sample belongs. Table IV shows the confusion matrix for the training set, including the percentage of producer accuracy (PA), user accuracy (UA), and the overall accuracy (OA) using the DTW similarity

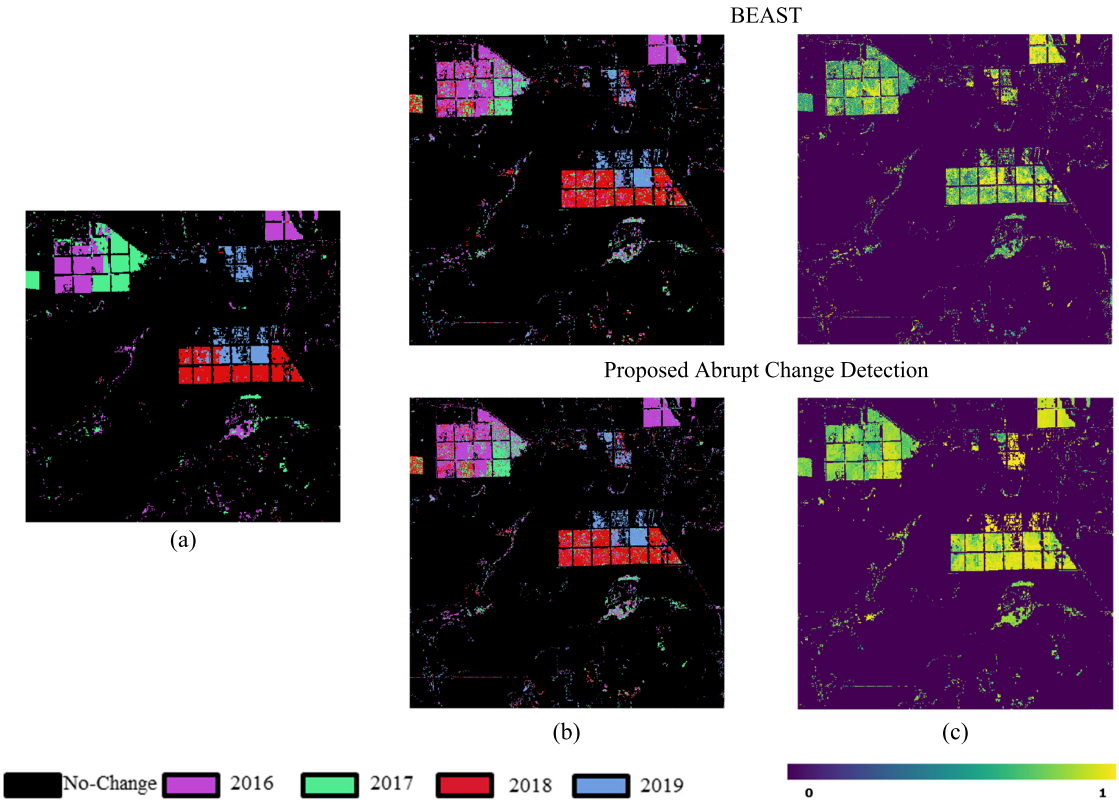

Fig. 6. (a) Change reference map with the year of the change. (b) Abrupt change maps with the indication of the year of the change and (c) Probability of change for BEAST (top) and the proposed approach (bottom).

measure. OA is approximately 68% that represents a good percentage of accurate predictions for the training set.

P_A and P_B have been established according to a robustness analyses. The parameter sensitivity analysis was conducted using a subset (30%) of samples per class. The optimal value of the most influential parameters P_A and P_B were gradually increased and decreased in the range [10%, 50%] and the accuracy calculated (Fig. 5). The method resulted to be stable across varying parameter settings.

C. Results on Testing Dataset 1

To proceed with the detection of the LC transitions, the steps regarding the feature selection, PCC masking, time series reconstruction, and MHCVA were implemented on testing dataset 1. The proposed abrupt CD was applied to further exclude unchanged pixels from the testing set. For this analysis, the parameter "h" representing the minimal segment size between potentially detected breaks, is configured to 0.25, while the number of breaks is set to 1, and the maximum number of iterations is restricted to 1. The output of the abrupt CD together with the reference map are visualized in Fig. 6 where the year of the change and the probability of change are reported for each pixel. Considering the sample images in Fig. 3 and the maps in Fig. 6, the growth of the crop fields is observable during the considered period. To assess the performance, a quantitative analysis is provided in terms of false and missed alarms (Table V). Furthermore, the abrupt CD module is compared with Bayesian estimator of abrupt change, seasonal change, and trend (BEAST)

TABLE V
OVERALL FALSE/MISSED ALARMS

Method	False Alarms% (pixels)	Missed Alarms% (pixels)
BEAST	8.62%	5.99%
Proposed Abrupt Change Detection	8.01%	5.57%

[43]. Both proposed abrupt CD and BEAST demonstrate a good performance in detecting the year of change. While BEAST offers flexible representation and can handle irregular data, it is not well-suited for dense HR data due to its computationally intensive Bayesian calculations. The abrupt CD module not only exhibits lower false/missed alarms but also showcases a significantly faster processing time, being approximately three times faster than BEAST, considering a Python implementation. Furthermore, the reported probability as a measure of uncertainty associated with detected change exhibits higher levels of confidence for the proposed abrupt CD. To produce the LC transition map, the DTW similarity measure was computed between the TS_p^{Te} discretized into 1-year period and CPs (Section II-F). Fig. 7 shows the reference DW LC maps for each year and the generated LC transition maps for the testing dataset 1. The main transition is from trees to grassland/cropland, which occurs in various locations between 2016 and 2019. Fig. 7 clearly shows the changes (green color to yellow/orange color). In the top left side of the area, two LC transitions can be observed, characterized

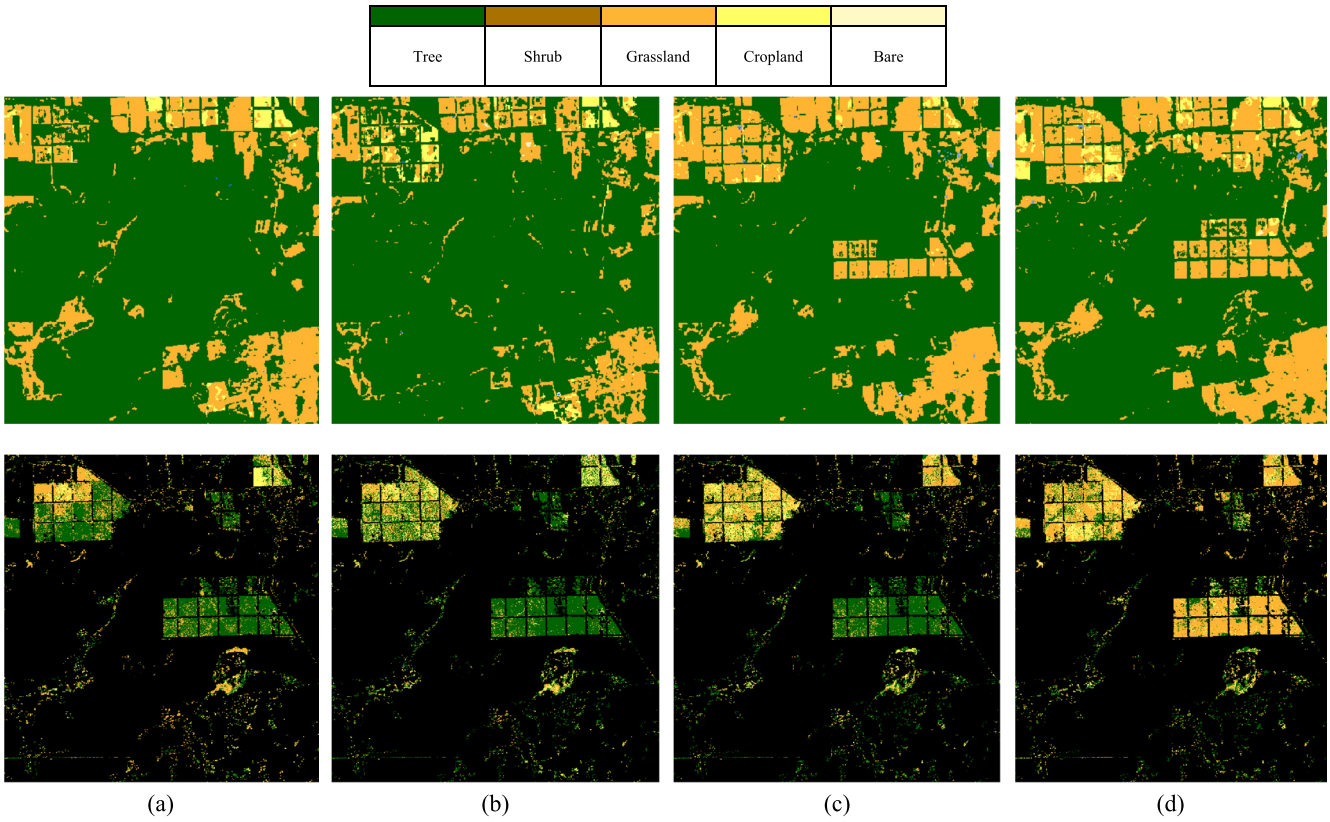

Fig. 7. Reference maps (top) and CD maps (bottom) of the first testing dataset for (a) 2016, (b) 2017, (c) 2018, and (d) 2019.

TABLE VI
JACCARD INDEX AND BF SCORE FOR EACH YEAR BETWEEN THE REFERENCE MAP AND THE PROPOSED APPROACH

	Jaccard Index	BF Score
2016	0.7788	0.6378
2017	0.7701	0.6261
2018	0.6737	0.5080
2019	0.7005	0.5391

TABLE VII
TIME COMPLEXITY FOR THE TRAINING AND TESTING DATASET 1

Module	100px × 100px minutes
Feature Extraction	0.05
Time Series Reconstruction	4
Abrupt Change Detection	28
DTW LC-Driven Training	1345
LC Classification and CD	205

by the initiation of crop field construction in 2016 and its completion in 2019. Another transition is located in the center of the area, occurring between 2018 and 2019.

To assess the quantitative performance, two metrics are considered: Jaccard index (or intersection over union) [38] and Boundary F1 (BF) score [39]. The indices range in the [0, 1], where 0 indicates no agreement between the reference map and the CD map, and 1 indicates complete agreement. The level of agreement between the reference maps and the ones generated using the proposed method is represented in Table VI. The level of agreement for both Jaccard index and BF score is high meaning that the proposed approach has a reliable performance.

We performed an additional analysis to evaluate the computational burden of the proposed approach for training and testing set 1. This is done on an Intel Core i7-7700 CPU running at 3.60 GHz with 32 GB of RAM, which is detailed for a 100 × 100 area for each module in the processing chain (Table VII). The abrupt CD module is quite fast, taking 25 min to detect changes for 100 × 100 area. The LC transition detection module computational time takes 205 min. The supervised nature of the method and the volume of processed pixels contribute to the longer processing times. However, the prototypes generated through this method can be utilized to analyze different areas for studying different LC changes. Moreover, the accuracy and precision of the results make this approach suitable for applications such as crop monitoring and climate change studies.

D. Results on Testing Dataset 2

Fig. 8 shows the LC transition map together with DW reference map for the testing dataset 2. The LC transition map indicates transitions from bare to build up and crop that have been properly detected by the proposed approach. The quantitative analysis in terms of Jaccard index and average BF score demonstrated a high level of concordance (Table VIII).

This points out that once the CPs or LC models are established, they can be applied to other areas. This highlights the generalizability of the proposed method for broader applications.

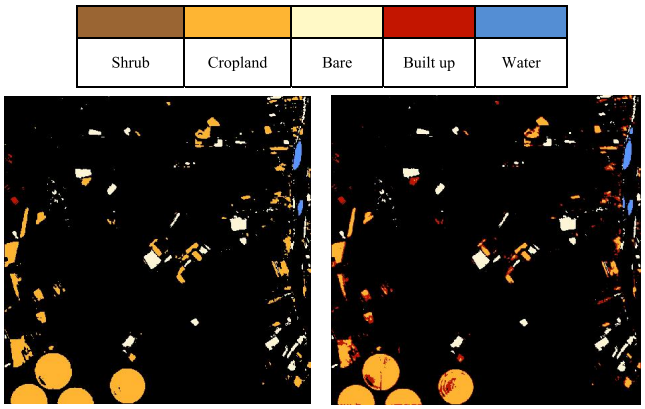

Fig. 8. (a) Reference map and (b) LC transition map for testing dataset 2.

TABLE VIII
JACCARD INDEX AND BF SCORE BETWEEN THE REFERENCE MAP AND THE PROPOSED APPROACH FOR TESTING DATASET 2

	Jaccard Index	BF Score
2016	0.7802	0.6924

IV. CONCLUSION

This study has addressed some of the limitations of existing LCC detection methods by proposing a novel approach that utilizes HR SITS to analyze LC dynamics over several years. By exploiting the spatial, spectral, and temporal information captured in the SITS data, our approach offers a comprehensive understanding of LCCs and provides detailed insights into the type of LC transition. It uses multiannual multispectral SITS to construct a multifeature hypertemporal FS, enabling the generation of CD maps that indicate the timing, probability, and specific type of changes. Through experimental evaluations using multiannual Landsat 7 and 8 SITS data from 2015 to 2019 in an area of the Amazon region and from 2015 to 2016 in Sahel-Africa, we have demonstrated the effectiveness of the proposed approach in detecting multiannual LCCs and identifying the specific LC transitions. The outcomes of this research highlight the potential of HR SITS data and of the proposed approach for comprehensive and detailed analysis of LCCs. Compared with previous studies, the proposed abrupt CD method demonstrates superior performance, particularly notable for its reduced time demand. Additionally, the LC transition detection method sets it apart from existing methods in properly detecting LC transitions using multiannual SITS. This has significant implications for various applications, including environmental monitoring, urban planning, and climate change.

As future development, we aim to reduce the complexity and computational burden of the proposed approach. Additionally, we plan to expand the application of the proposed approach to different geographical regions and LC types to further analyze its generalizability and effectiveness across diverse environments. Moreover, while this article focuses on annual LC CD, there is potential to explore finer temporal resolutions, such as monthly or seasonal changes.

REFERENCES

[1] J. Verbesselt, A. Zeileis, and M. Herold, "Near real-time disturbance detection using satellite image time series," *Remote Sens. Environ.*, vol. 123, pp. 98–108, Aug. 2012, doi: 10.1016/j.rse.2012.02.022.
[2] M. Decuyper et al., "Continuous monitoring of forest change dynamics with satellite time series," *Remote Sens. Environ.*, vol. 269, Feb. 2022, Art. no. 112829, doi: 10.1016/j.rse.2021.112829.
[3] D. Lu, E. Moran, and S. Hetrick, "Detection of impervious surface change with multitemporal Landsat images in an urban–rural frontier," *ISPRS J. Photogramm. Remote Sens.*, vol. 66, no. 3, pp. 298–306, May 2011.
[4] S. Stramondo, C. Bignami, M. Chini, N. Pierdicca, and A. Tertulliani, "Satellite radar and optical remote sensing for earthquake damage detection: Results from different case studies," *Int. J. Remote Sens.*, vol. 27, no. 20, pp. 4433–4447, Oct. 2006.
[5] K. Meshkini, F. Bovolo, and L. Bruzzone, "A 3D CNN approach for change detection in HR satellite image time series based on a pretrained 2D CNN," *Int. Arch. Photogramm., Remote Sens. Spatial Inf. Sci.*, vols. 43, pp. 143–150, May 2022.
[6] A. Rodrigues, A. R. S. Marcal, and M. Cunha, "Monitoring vegetation dynamics inferred by satellite data using the PhenoSat tool," *IEEE Trans. Geosci. Remote Sens.*, vol. 51, no. 4, pp. 2096–2104, Apr. 2013, doi: 10.1109/TGRS.2012.2223475.
[7] Y. T. Solano-Correa, F. Bovolo, L. Bruzzone, and D. Fernández-Prieto, "A method for the analysis of small crop fields in Sentinel-2 dense time series," *IEEE Trans. Geosci. Remote Sens.*, vol. 58, no. 3, pp. 2150–2164, Mar. 2020, doi: 10.1109/TGRS.2019.2953652.
[8] C. Senf, D. Pflugmacher, M. A. Wulder, and P. Hostert, "Characterizing spectral–temporal patterns of defoliator and bark beetle disturbances using Landsat time series," *Remote Sens. Environ.*, vol. 170, pp. 166–177, Dec. 2015.
[9] A. Asokan and J. Anitha, "Change detection techniques for remote sensing applications: A survey," *Earth Sci. Inform.*, vol. 12, no. 2, pp. 143–160, Jun. 2019, doi: 10.1007/s12145-019-00380-5.
[10] G. Jianya, S. Haigang, M. Guorui, and Z. Qiming, "A review of multi-temporal remote sensing data change detection algorithms," *Int. Arch. Photogramm., Remote Sens. Spatial Inf. Sci.*, vol. 37, no. B7, pp. 757–762, 2008.
[11] I. Pôças, M. Cunha, A. R. S. Marcal, and L. S. Pereira, "An evaluation of changes in a mountainous rural landscape of Northeast Portugal using remotely sensed data," *Landscape Urban Planning*, vol. 101, no. 3, pp. 253–261, Jun. 2011, doi: 10.1016/j.landurbplan.2011.02.030.
[12] X. Zhang, P. Xiao, X. Feng, and M. Yuan, "Separate segmentation of multi-temporal high-resolution remote sensing images for object-based change detection in urban area," *Remote Sens. Environ.*, vol. 201, pp. 243–255, Nov. 2017, doi: 10.1016/j.rse.2017.09.022.
[13] G. Vivekananda, R. Swathi, and A. Sujith, "Multi-temporal image analysis for LULC classification and change detection," *Eur. J. Remote Sens.*, vol. 54, no. 2, pp. 189–199, Mar. 2021, doi: 10.1080/22797254.2020.1771215.
[14] B. Wang, J. Choi, S. Choi, S. Lee, P. Wu, and Y. Gao, "Image fusion-based land cover change detection using multi-temporal high-resolution satellite images," *Remote Sens.*, vol. 9, no. 8, p. 804, Aug. 2017, doi: 10.3390/rs9080804.
[15] S. Jamali, P. Jönsson, L. Eklundh, J. Ardö, and J. Seaquist, "Detecting changes in vegetation trends using time series segmentation," *Remote Sens. Environ.*, vol. 156, pp. 182–195, Jan. 2015, doi: 10.1016/j.rse.2014.09.010.
[16] W. B. Cohen, Z. Yang, and R. E. Kennedy, "Detecting trends in forest disturbance and recovery using yearly Landsat time series: 1. LandTrendr—Temporal segmentation algorithms," *Remote Sens. Environ.*, vol. 114, no. 12, pp. 2897–2910, 2010.
[17] R. De Jong, J. Verbesselt, M. E. Schaepman, and S. De Bruin, "Trend changes in global greening and browning: Contribution of short-term trends to longer-term change," *Global Change Biol.*, vol. 18, no. 2, pp. 642–655, 2012.
[18] E. B. Brooks, R. H. Wynne, V. A. Thomas, C. E. Blinn, and J. W. Coulston, "On-the-fly massively multitemporal change detection using statistical quality control charts and Landsat data," *IEEE Trans. Geosci. Remote Sens.*, vol. 52, no. 6, pp. 3316–3332, Jun. 2014.
[19] J. Verbesselt, R. Hyndman, G. Newnham, and D. Culvenor, "Detecting trend and seasonal changes in satellite image time series," *Remote Sens. Environ.*, vol. 114, no. 1, pp. 106–115, Jan. 2010.
[20] J. Lambert, C. Drenou, J.-P. Denux, G. Balent, and V. Cheret, "Monitoring forest decline through remote sensing time series analysis," *GIScience Remote Sens.*, vol. 50, no. 4, pp. 437–457, Aug. 2013, doi: 10.1080/15481603.2013.820070.

[21] O. A. C. Júnior et al., "A new approach to change vector analysis using distance and similarity measures," *Remote Sens.*, vol. 3, no. 11, pp. 2473–2493, Nov. 2011, doi: 10.3390/rs3112473.
[22] F. Bovolo and L. Bruzzone, "A theoretical framework for unsupervised change detection based on change vector analysis in the polar domain," *IEEE Trans. Geosci. Remote Sens.*, vol. 45, no. 1, pp. 218–236, Jan. 2007.
[23] K. Meshkini, F. Bovolo, and L. Bruzzone, "A multi-feature hypertemporal change vector analysis method for change detection in multi-annual time series of HR satellite images," in *Proc. IEEE Int. Geosci. Remote Sens. Symp. (IGARSS)*, Jul. 2023, pp. 8315–8318.
[24] D. J. Berndt and J. Clifford, "Using dynamic time warping to find patterns in time series," in *Proc. KDD Workshop*, 1994, pp. 356–370.
[25] T. Rakthanmanon et al., "Searching and mining trillions of time series subsequences under dynamic time warping," in *Proc. 18th ACM SIGKDD Int. Conf. Knowl. Discovery Data Mining*, Aug. 2012, pp. 262–270.
[26] F. Petitjean, J. Inglada, and P. Gançarski, "Satellite image time series analysis under time warping," *IEEE Trans. Geosci. Remote Sens.*, vol. 50, no. 8, pp. 3081–3095, Aug. 2012.
[27] F. Petitjean and J. Weber, "Efficient satellite image time series analysis under time warping," *IEEE Geosci. Remote Sens. Lett.*, vol. 11, no. 6, pp. 1143–1147, Jun. 2014.
[28] M. Baumann, M. Ozdogan, A. D. Richardson, and V. C. Radeloff, "Phenology from Landsat when data is scarce: Using MODIS and dynamic time-warping to combine multi-year Landsat imagery to derive annual phenology curves," *Int. J. Appl. Earth Observ. Geoinf.*, vol. 54, pp. 72–83, Feb. 2017, doi: 10.1016/j.jag.2016.09.005.
[29] M. Belgiu and O. Csillik, "Sentinel-2 cropland mapping using pixel-based and object-based time-weighted dynamic time warping analysis," *Remote Sens. Environ.*, vol. 204, pp. 509–523, Jan. 2018, doi: 10.1016/j.rse.2017.10.005.
[30] *Google Earth Engine*. Accessed: May 20, 2023. [Online]. Available: https://developers.google.com/earth-engine/datasets/catalog/landsat
[31] M. Boschetti, F. Nutini, G. Manfron, P. A. Brivio, and A. Nelson, "Comparative analysis of normalised difference spectral indices derived from MODIS for detecting surface water in flooded Rice cropping systems," *PLoS ONE*, vol. 9, no. 2, Feb. 2014, Art. no. e88741, doi: 10.1371/journal.pone.0088741.
[32] L. Zhang, H. Su, and J. Shen, "Hyperspectral dimensionality reduction based on multiscale superpixelwise kernel principal component analysis," *Remote Sens.*, vol. 11, no. 10, p. 1219, May 2019.
[33] Y. T. Solano-Correa, K. Meshkini, F. Bovolo, and L. Bruzzone, "A land cover-driven approach for fitting satellite image time series in a change detection context," *Proc. SPIE*, vol. 11533, Sep. 2020, Art. no. 1153309, doi: 10.1117/12.2573942.
[34] T. Häme, L. Sirro, J. Kilpi, L. Seitsonen, K. Andersson, and T. Melkas, "A hierarchical clustering method for land cover change detection and identification," *Remote Sens.*, vol. 12, no. 11, p. 1751, May 2020, doi: 10.3390/rs12111751.
[35] Y. Yuan et al., "Development and application of a modified dynamic time warping algorithm (DTW-S) to analyses of primate brain expression time series," *BMC Bioinf.*, vol. 12, no. 1, p. 347, Dec. 2011, doi: 10.1186/1471-2105-12-347.
[36] P. K. Bhattacharya, "Estimation of a probability density function and its derivatives," *Sankhyā: Indian J. Statist., A*, vol. 29, pp. 373–382, 1967.
[37] *Landsat Collections in Earth Engine | Earth Engine Data Catalog*. Google Dev. Accessed: May 20, 2022. [Online]. Available: https://developers.google.com/earth-engine/datasets/catalog/landsat
[38] *Landsat Collection 2*. Accessed: Jun. 20, 2022. [Online]. Available: https://www.usgs.gov/landsat-missions/landsat-collection-2
[39] C. J. Crawford et al., "The 50-year Landsat collection 2 archive," *Sci. Remote Sens.*, vol. 8, Dec. 2023, Art. no. 100103, doi: 10.1016/j.srs.2023.100103.
[40] *Climate Change Initiative (CCI) Land-Cover and Change Detection Maps*. Accessed: May 21, 2024. [Online]. Available: https://climate.esa.int/en/news-events/high-resolution-maps-reveal-real-world-land-use-change/
[41] *Dynamic World*. Accessed: Jun. 5, 2023. [Online]. Available: https://dynamicworld.app/
[42] Y. T. Solano-Correa, K. Meshkini, F. Bovolo, and L. Bruzzone, "Automatic large-scale precise mapping and monitoring of agricultural fields at country level with Sentinel-2 SITS," *IEEE J. Sel. Topics Appl. Earth Observ. Remote Sens.*, vol. 15, pp. 3131–3145, 2022.
[43] K. Zhao et al., "Detecting change-point, trend, and seasonality in satellite time series data to track abrupt changes and nonlinear dynamics: A Bayesian ensemble algorithm," *Remote Sens. Environ.*, vol. 232, Oct. 2019, Art. no. 111181.

Khatereh Meshkini (Member, IEEE) received the master's degree in telecommunication engineering from Science and Research University, Tehran, Iran, in 2016, and the Ph.D. degree in information and computer science from the University of Trento, Trento, Italy, in 2024.

She is currently a Post-Doctoral position with the Remote Sensing for Digital Earth Unit, Fondazione Bruno Kessler, Trento, and with the Remote Sensing Laboratory, Department of Information and Communication Technologies, University of Trento. She has been involved in projects developing advanced methods for high-resolution satellite image analysis, such as Scientific Exploitation of Operational Missions (SEOM), S2-4Sci Land and Water, Multi-temporal Analysis and CCI+, High Resolution Landcover Climate Change Initiative–funded by ESA, where she is developing new methods to detect land cover changes in different areas of the world. She is the author or co-author of several scientific publications in both international conferences and journals. Her research interests lie in multitemporal remote sensing image analysis, change detection in medium resolution (e.g., Landsat, Sentinel-2) and very high-resolution (VHR) images, deep neural networks for satellite image processing, image classification, and information extraction.

Dr. Meshkini was a Best Student Paper finalist at the IEEE International Geoscience and Remote Sensing Symposium (IGARSS) in 2023 and 2024.

Yady Tatiana Solano-Correa (Member, IEEE) received the B.S. degree in physics engineering (Hons.) from the University of Cauca, Cauca, Colombia, in 2011, and the Ph.D. degree (magna cum laude) in communication and information technologies from the Department of Information Engineering and Computer Science, University of Trento, Trento, Italy, in 2018.

From 2009 to 2013, she was a Researcher for the research groups: Optics and Laser Group (GOL) and Environmental Studies Group (GEA), University of Cauca. From 2013 to 2020, she was a Researcher for the Remote Sensing for Digital Earth Unit, Fondazione Bruno Kessler, Trento, and a member of the RSLab, University of Trento. From 2020 to 2024, she was a Professor at The Universidad Tecnológica de Bolívar, Colombia, and a Researcher at the University of Cauca. She is currently a Professor in data science at the Pontificia Universidad Javeriana, Bogotá, Colombia. She works, and has worked, within the context of several projects with a focus on analyzing/processing information for climate change, precision agriculture, water security, and developing advanced change detection techniques for optical satellite time series data, among them: 1) RICCLISA—Interinstitutional network of climate change and food security, Colombia. Founded by the Colombian administrative department of Science, Technology and Innovation—COLCIENCIAS; 2) MS-TS-Analysis of MultiSensor VHR image Time Series, in collaboration with Digital Globe Foundation; 3) SEOM-Scientific Exploitation of Operational Missions-S2-4Sci Land and Water-Multitemporal Analysis. Founded by European Space Agency (ESA); 4) CCI+ HR LC - High Resolution Land Cover Essential Climate Variable. Founded by ESA; 5) SHARE-Desarrollo de Estrategias de Seguridad Hídrica y Alimentaria para la Reactivación Económica en comunidades rurales mediante transferencia de tecnología y conocomientos para la innovación como medida de atención a la emergencia del COVID-19 en el Cauca, Founded by MinCiencias in Colombia; and 6) Water Security for sustainable development HUB, founded by UKRI and GCRF. Her research interests include data science and remote sensing environmental applications, change detection, both on medium-resolution multispectral images (e.g., Landsat and Sentinel-2) and very high-resolution (VHR) images, multitemporal analysis of short- and long-time series, multisensor multitemporal image preprocessing and information extraction, pattern recognition, and image classification.

Dr. Solano-Correa was a recipient of the Best Student Oral Presentation Award at the MultiTemp 2017 Conference, Bruges, Belgium, in 2017, and the Best three Ph.D. thesis presented in 2018 and 2019 in the area of Geoscience and Remote Sensing (GRS), in Italy. She has been reviewer for the IEEE International Geoscience and Remote Sensing Symposium (IGARSS) and other international conferences. She is a referee for IEEE TRANSACTIONS ON GEOSCIENCE AND REMOTE SENSING, IEEE JOURNAL OF SELECTED TOPICS IN APPLIED EARTH OBSERVATIONS AND REMOTE SENSING, IEEE GEOSCIENCE AND REMOTE SENSING LETTERS, and several other international journals.

Francesca Bovolo (Senior Member, IEEE) received the Laurea (B.S.) degree, the Laurea Specialistica (M.S.) degree (summa cum laude) in telecommunication engineering, and the Ph.D. degree in communication and information technologies from the University of Trento, Trento, Italy, in 2001, 2003, and 2006, respectively.

She was a Research Fellow with the University of Trento until 2013. She is currently the Founder and the Head of Remote Sensing for Digital Earth Unit, Fondazione Bruno Kessler, Trento, and a member of the Remote Sensing Laboratory, Trento. She is one of the co-investigators of the Radar for Icy Moon Exploration instrument of the European Space Agency Jupiter Icy Moons Explorer and member of the Science Study Team of the EnVision mission to Venus. Her research interests include remote-sensing image processing, multitemporal remote sensing image analysis, change detection in multispectral, hyperspectral, and synthetic aperture radar images, and very high-resolution images, time series analysis, content-based time series retrieval, domain adaptation, and light detection and ranging (LiDAR) and radar sounders. She conducts research on these topics within the context of several national and international projects.

Dr. Bovolo is a member of the program and scientific committee of several international conferences and workshops. She was a recipient of the First Place in the Student Prize Paper Competition of the 2006 IEEE International Geoscience and Remote Sensing Symposium, Denver, in 2006. She was the Technical Chair of the Sixth International Workshop on the Analysis of Multitemporal Remote-Sensing Images (MultiTemp 2011 and 2019). She has been a Co-Chair of the SPIE International Conference on Signal and Image Processing for Remote Sensing since 2014. She is the Publication Chair of the International Geoscience and Remote Sensing Symposium in 2015. She has been an Associate Editor of IEEE JOURNAL OF SELECTED TOPICS IN APPLIED EARTH OBSERVATIONS AND REMOTE SENSING since 2011 and the Guest Editor of the Special Issue on Analysis of Multitemporal Remote Sensing Data of IEEE TRANSACTIONS ON GEOSCIENCE AND REMOTE SENSING. She is a referee for several international journals.

Lorenzo Bruzzone (Fellow, IEEE) received the Laurea (M.S.) degree in electronic engineering (summa cumlaude) and the Ph.D. degree in telecommunications from the University of Genoa, Italy, in 1993 and 1998, respectively.

He is currently a Full Professor of telecommunications at the University of Trento, Trento, Italy, where he teaches remote sensing, radar, and digital communications, where he is the Founder and the Director of the Remote Sensing Laboratory (https://rslab.disi.unitn.it/), Department of Information Engineering and Computer Science. He is the Principal Investigator of many research projects. Among the others, he is currently the Principal Investigator of the Radar for icy Moon exploration (RIME) instrument in the framework of the JUpiter ICy Moons Explorer (JUICE) mission of the European Space Agency (ESA) and the Science Lead for the High Resolution Land Cover project in the framework of the Climate Change Initiative of ESA. He has author (or co-author) of more than 390 scientific publications in referred international journals, more than 390 papers in conference proceedings, and 22 book chapters. He is editor/coeditor of 18 books/conference proceedings and one scientific book. His research interests are in the areas of remote sensing, radar and SAR, signal processing, machine learning, and pattern recognition. He promotes and supervises research on these topics within the frameworks of many national and international projects.

Dr. Bruzzone has been a member of the Administrative Committee of the IEEE Geoscience and Remote Sensing Society (GRSS) since 2009, where he has been the Vice President for Professional Activities since 2019. He ranked first place in the Student Prize Paper Competition of the 1998 IEEE International Geoscience and Remote Sensing Symposium (IGARSS), Seattle, July 1998. Since that he was recipient of many international and national honors and awards, including among the most recent ones the IEEE GRSS 2015 Outstanding Service Award, the 2017 and 2018 IEEE IGARSS Symposium Prize Paper Awards, and the 2019 WHISPER Outstanding Paper Award and the 2022 Letter Prize Paper Award for the best paper published on the IEEE GEOSCIENCE AND REMOTE SENSING LETTERS in 2022. He was a guest coeditor of many Special Issues of international journals. He is the Co-Founder of the IEEE International Workshop on the Analysis of Multi-Temporal Remote-Sensing Images (MultiTemp) series and is currently a member of the Permanent Steering Committee of this series of workshops. Since 2003, he has been the Chair of the SPIE Conference on Image and Signal Processing for Remote Sensing. He has been the Founder of the *IEEE Geoscience and Remote Sensing Magazine* for which he has been the Editor-in-Chief from 2013 to 2017. He is currently an Associate Editor for the IEEE TRANSACTIONS ON GEOSCIENCE AND REMOTE SENSING. His papers are highly cited, as proven from the total number of citations (more than 50000) and the value of the H-index (106) (source: Google Scholar). He was invited as keynote speaker in more than 40 international conferences and workshops. He has been Distinguished Speaker of the IEEE Geoscience and Remote Sensing Society from 2012 to 2016.